THE JOURNAL OF PHYSICAL CHEMISTRY C
A JOURNAL OF THE AMERICAN CHEMICAL SOCIETY

pubs.acs.org/JPCC

Article

Electronic Structure of Anode Material Li_2TiSiO_5 and Its Structural Evolution during Lithiation

Yifan Wu, Zhenming Xu, Yao Liu, Junchao Chen, Luming Peng, Olaf J. Borkiewicz, Hong Zhu,* Shou-Hang Bo,* and Yongyao Xia*

Cite This: *J. Phys. Chem. C* 2021, 125, 3733−3744

Read Online

ACCESS | Metrics & More | Article Recommendations | Supporting Information

ABSTRACT: Inductive effect, although originally proposed in the field of organic chemistry, has long been regarded as an effective way to increase the working potential of inorganic lithium-ion battery cathodes. A classic example is the $LiFePO_4$ cathode, where introduction of the highly electronegative P^{5+} raises the redox potential of Fe^{3+}/Fe^{2+} as in conventional oxides by 1.0 V. Recently, some of us have reported a substantially reduced redox potential of Ti^{4+}/Ti^{3+} in Li_2TiSiO_5 compared with lithium titanium oxides, suggesting the presence of a reversed inductive effect imposed by polyanions (*Energy Environ. Sci.*, **2017**, *10*, 1456−1464). In this work, through characterizing the electronic structure of pristine Li_2TiSiO_5 and following the crystallographic structure evolution during lithium insertion in Li_2TiSiO_5, we propose that the reversed inductive effect is likely linked with the square-pyramid coordination of Ti. The reversed inductive effect offers new possibilities in tuning the potentials of anode materials, presenting a promising avenue to further increase the energy density of batteries based on polyanion electrodes.

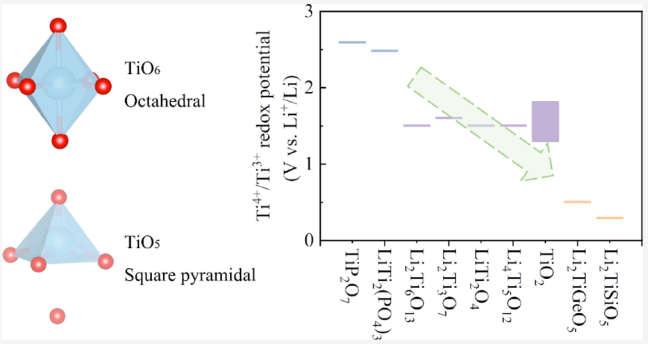

INTRODUCTION

Batteries are playing a more vital role than ever in various aspects of human life, for example, communication, transportation, and illumination. Lithium-ion batteries (LIBs) have been the dominant contender in the battery market over the past few decades. However, in spite of relatively high energy density compared with other energy storage alternatives, higher energy density of LIBs is still required for a more sustainable energy future.

Energy density of a LIB cell directly relates to the electrochemical potential difference between the cathode and the anode. Tuning the electrochemical potentials of the cathode and anode materials is therefore extremely important. In 1997, Padhi and co-workers reported phospho-olivines as cathode materials for LIBs.[1,2] In $LiFePO_4$ and in $LiFe_{1-x}Mn_xPO_4$ solid-solution materials, the electrochemical potentials of Fe^{3+}/Fe^{2+} and Mn^{3+}/Mn^{2+} redox couples were observed to be 3.5 and 4.1 V versus Li^+/Li, respectively, which are much higher than those in typical lithium iron oxides (2.4−3.0 V[3−5]) and lithium manganese oxides (<3.0 V[6,7]). In later reports, Padhi *et al.* systematically mapped out the electrochemical potentials of Fe^{3+}/Fe^{2+} redox couples in structures with different polyanions.[8,9] A strong correlation was identified between the electrochemical potential of Fe^{3+}/Fe^{2+} redox couple and the electronegativity of the central atom in the polyanion, providing an effective way to tune the electrochemical potentials of battery cathode materials.

The increase of electrochemical potentials in Fe^{3+}/Fe^{2+} redox couples compared with those in simple lithium iron oxides was attributed to the inductive effect introduced by the polyanion. The inductive effect was initially proposed as a model to describe the successive polarization of chemical bonds between the start (substituent) and the end (reaction site) on molecular skeleton of polymers.[10,11] Later, the inductive effect was extended to inorganic materials by Noll to rationalize the bonding characters and chemical behavior of metal-containing silicates with the presence of M−O−Si connectivity (M stands for metal).[12] The strength of the inductive effect is related to the electronegativity difference between M and Si, which determines the chemical behavior of metal-containing silicates to a large extent. In phosphate cathode materials such as those reported by Padhi and co-workers, O atom bridges P^{5+} and Fe^{2+} cations (*i.e.*, Fe−O−P connectivity). Higher electronegativity of P^{5+} compared with

Received: November 12, 2020
Revised: January 28, 2021
Published: February 12, 2021

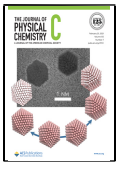

Fe^{2+} pulls electrons from the bridging O atom. This induces further electron redistribution toward O atom in the Fe−O σ bond, reducing Fe−O bond covalency or effective overlap between Fe and O electron clouds. Less covalency in the Fe−O bond caused by the inductive effect of the phosphate group results in an increase in electrochemical potential. Similar voltage increase has been verified in various polyanion cathode materials.[1,9,13−18]

Electrochemical potentials of the anode materials also require optimization. Lithium metal with the lowest electrochemical potential is considered as the most energy-dense battery anode. However, the practical application of the lithium metal anode is still plagued by inhomogeneous lithium plating and stripping during battery charge and discharge processes, which can lead to catastrophic failure of batteries.[19] Higher up in the electrochemical potential diagram are carbonaceous anodes with an average working potential of 0−0.3 V versus Li^+/Li.[20−24] However, such a low working potential can still lead to lithium plating under abuse conditions such as high current density (*e.g.*, fast charging) and extreme temperatures, posing safety hazards.[25−28] Anodes based on alloying reactions with lithium, such as Si,[29,30] Ge,[31,32] and Sn,[33] operate at higher electrochemical potentials (below 1 V *vs* Li^+/Li) and are free of safety risks associated with lithium metal plating. Nevertheless, Coulombic efficiency of alloy anodes is still low because of continuous side reactions between the electrode and liquid electrolyte.[34,35] Titanium-based anode materials that operate based on Ti^{4+}/Ti^{3+} redox couple generally show high cycling stability, Coulombic efficiency, and safety. However, these attributes are achieved at the expense of energy density. For example, the well-known "zero-strain" anode material $Li_4Ti_5O_{12}$ exhibits a working potential of 1.5 V versus Li^+/Li,[36] making it difficult to be utilized in high-energy density batteries. Other titanium-based anode materials ($LiTi_2O_4$,[37,38] $Li_2Ti_3O_7$,[39,40] and $Li_2Ti_6O_{13}$[41,42]) are facing similar challenges.

A strategy that reduces the electrochemical potentials of titanium-based anode materials, similar to the inductive effect in polyanion cathodes, is needed. In 2002, Patoux and Masquelier investigated a number of titanium-based polyanion anode materials, aiming to uncover the correlation among the crystal structure, the nature of polyanion group, and electrochemical performance.[43] Titanate anode materials containing PO_4^{3-}, $P_2O_7^{4-}$, SO_4^{2-}, and SiO_4^{4-} polyanions were compared. While almost all materials show similar or higher voltage than those of lithium titanium oxides (*e.g.*, $LiTi_2O_4$, $Li_2Ti_3O_7$, and $Li_4Ti_5O_{12}$) consistent with predictions from the inductive effect of polyanions, Li_2TiSiO_5 with a square-pyramid Ti coordination is an exception. Li_2TiSiO_5 unexpectedly showed lower electrochemical potential (less than 1 V *vs* Li^+/Li on average) than lithium titanium oxides, in stark contrast to common expectation based on the inductive effect of silicate groups. Furthermore, only 0.15 Li per formula can be reversibly cycled within 1−3 V versus Li^+/Li with a limited capacity of 23.7 mA h g^{-1}. In 2017, some of us revisited Li_2TiSiO_5 by employing submicron particles with a few nanometers of carbon coating. This optimized material showed an extremely low electrochemical potential of 0.28 V versus Li^+/Li on average and large reversible capacity (308 mA h g^{-1}), suggesting a two-electron process with Ti^{4+} reduction to Ti^{2+} or even below.

The lithiation process of Li_2TiSiO_5 was characterized by *in situ* and *ex situ* X-ray diffraction, X-ray absorption near-edge structure analysis (XANES), and density functional theory (DFT) modeling.[44] A complex mechanism of sequential intercalation and conversion was proposed. Lithiated $Li_{2+x}TiSiO_5$ was first formed at the beginning of discharge. A conversion of lithiated $Li_{2+x}TiSiO_5$ into Li_4SiO_4 and TiO was evidenced in the middle of discharge. The last stage of lithiation was postulated to be an intercalation process forming Li_xTiO. However, due to the lack of direct evidence confirming the Ti oxidation state or Li local environment, the formation of intercalated Li_xTiO remains uncertain.

Furthermore, while the operating potential of Li_2TiSiO_5 fills the gap between carbonaceous and lithium titanate anodes and is ideal for battery anode applications, the mechanism for electrochemical potential reduction of Ti^{4+}/Ti^{3+} redox couple still remains elusive. Unraveling such a mechanism is necessary to rationalize strategies for systematic tuning of electrochemical potentials for battery anodes.

In the present work, we characterized the electronic structure of pristine Li_2TiSiO_5 and followed the crystallographic structural evolution during lithium insertion in Li_2TiSiO_5, shedding lights into the fundamental origin of the observed low working potential. The electronic structure of Li_2TiSiO_5 was characterized through density of states (DOS) calculation and crystal orbital Hamilton population (COHP) analysis *via* DFT modeling. The structural information was probed through pair distribution function (PDF) analysis, ^7Li solid state nuclear magnetic resonance (NMR) spectroscopy, and X-ray absorption fine structure (XAFS) analysis. It was observed that the titanium atom gradually shifts to the center of the basal plane of the square pyramid resembling a distorted octahedral coordination during topotactic lithium insertion. Finally, on the basis of the reversed inductive effect (electrochemical potential reduction rather than increase in the conventional inductive effect), we discussed the possibility to tune the electrochemical potentials in Li_2TiMO_5 materials (M represents 4^+ cation) and suggested new materials which can be explored as low-potential lithium- and sodium-ion battery anodes.

EXPERIMENTAL METHODS

Synthesis. Starting materials of preparing Li_2TiSiO_5 in a liquid-state approach were tetrabutyl titanate (AR, Alfa Aesar), tetraethyl orthosilicate (AR, Alfa Aesar), and LiOH (AR, Sinopharm). Identical amounts of tetrabutyl titanate (0.02 mol) and tetraethyl orthosilicate (0.02 mol) were first dissolved and magnetic stirred in 40 mL of ethanol until complete dissolution. With continuous stirring, 80 mL of LiOH aqueous solution (0.04 mol) was added into the mixture, obtaining a white suspension. Further by rotatory evaporation of the suspension at a temperature of 50 °C, white powder was collected. The white powder was placed into a corundum boat afterward. Li_2TiSiO_5 powder can be obtained after heating at 870 °C in a muffle furnace for 8 h under an argon atmosphere. The temperature was heated to 870 °C under a ramping rate of 5 °C min^{-1} and cooled to room temperature under the same rate. The product then underwent ball milling under a frequency of 250 rpm for 100 min in total. Carbon coating at last was induced by a toluene flow under an argon atmosphere at the same temperature (*i.e.*, 870 °C).

Electrochemistry. The Li_2TiSiO_5 electrode for electrochemical measurements was prepared by mixing the active material Li_2TiSiO_5, carbon black (battery-class Super P, M.M.M.CarbonBelgium) and polyvinyl difluoride (battery-

https://dx.doi.org/10.1021/acs.jpcc.0c10221
J. Phys. Chem. C 2021, 125, 3733−3744

class, Arofina) dissolved in *N*-methyl-2-pyrrolidone (AR, Sinopharm) in a weight proportion of 8:1:1. The slurry was then casted onto a copper substrate by the doctor blade method, with a mass loading of approximately 5.3 mg cm^{-2}. After vacuum drying at 80 °C for 12 h, the electrode film was cut into 12 mm diameter circular pieces for coin cell assembly.

Half-cells were assembled in CR2016-type coin cells under an argon atmosphere in a glovebox. Functional parts of half-cells were layered in a sequence of the as-prepared electrode, a Celgard separator (Celgard 2400, Celgard), and a lithium metal foil (AR, China Energy Lithium). The electrolyte used in electrochemical tests was 1 M $LiPF_6$ (AR, Sigma-Aldrich) in ethylene carbonate/diethyl carbonate/dimethyl carbonate with 1:1:1 volumetric ratio. Cycling was performed with a NEWARE CT-4000 battery test system at a specific current of 5 mA g^{-1}. Cut off voltages of electrochemical tests were set to 0−3 V.

X-ray Scattering. X-ray total scattering data for PDF analysis were collected at the beamline 11-ID (λ = 0.21130 Å) at the Argonne National Laboratory. Samples for data collection were secured in quartz capillary tubes with an outer diameter of 0.9 mm under an argon atmosphere in a glovebox. The quartz capillaries were sealed with epoxy and then filled into polyimide capillaries (inner diameter 1.0 mm, outer diameter 1.1 mm).

The crystallography reported by Liu *et al.* was adopted as the initial structural model for PDF refinement.[44] Using GSAS-II[45] and PDFgui,[46] the PDF was derived from total scattering and refined. For the Fourier transform, a maximum scattering vector (Q_{max}) of 23.99 $Å^{-1}$ was adopted. Parameters including scale factor, lattice parameters, atomic coordinates, and isotropic atomic displacement parameters were fitted during refinement in a distance range of 1.0−30.0 Å.

X-ray Absorption Fine Structure. XAFS measurements were conducted at the beamline BL14W1 of Shanghai Synchrotron Radiation Facility (SSRF) for Ti K-edge in the transmission mode. The detector utilized during measurements was Si(111). Calibration of energy was conducted with a titanium foil, with the first inflection point fixed at 4966.0 eV. Extended XAFS (EXAFS) data were processed by the software Athena and Artemis.[47] By fitting a distorted octahedral model of the Ti−O coordination environment within a *R*-range of 1.2−3.0 Å, Ti−O interatomic distances were derived for samples at various state-of-charges along.

^{7}Li NMR. ^{7}Li magic angle spinning NMR (^{7}Li MAS NMR) experiments were recorded on Bruker AVANCE III 400 equipped with 89 mm wide-bore 9.4 T superconducting magnets in 1.3 mm rotors at Larmor frequencies of 155.5 MHz. Spinning speed of 50 kHz and repetition time of 4 s were used for accumulation of 320 scans for ^{7}Li single pulse spectrum. ^{7}Li chemical shift was referenced to 1 M LiCl solution recorded at 0 ppm.

COMPUTATIONAL METHODS

All calculations were carried out by using the projector augmented wave (PAW) method in the framework of the DFT,[48] as implemented in the Vienna ab initio simulation package. The generalized gradient approximation (GGA) and Perdew−Burke−Ernzerhof exchange functional[48] were used. The plane-wave energy cutoff was set to 520 eV, and the Monkhorst−Pack method[49] with a *k*-point mesh of 4 × 4 × 6 was employed for the Brillouin zone sampling of Li_2TiSiO_5. To consider the strong correlation effects of the transition metal Ti, the structural optimizations and DOS calculations were performed by using the spin-dependent GGA plus Hubbard correction *U* (GGA + *U*) method.[50] The Hubbard *U* parameter of Ti atom was set to 2.5 eV based on the previous study.[51] The convergence criteria of energy and force calculations was set to 10^{-5} eV $atom^{-1}$ and 0.01 eV $Å^{-1}$, respectively.

The COHP between titanium atom and neighboring oxygen atoms was computed by the Lobster program,[52] in which the positive or negative [−COHP] value indicates bonding ([−COHP] > 0) or antibonding ([−COHP] < 0), respectively. The pbeVaspFit2015 basis sets were used in the reconstruction of the PAW wave functions of Li, Ti, Si, and O atoms.

RESULTS

Crystallographic and Electronic Structure of Pristine Li_2TiSiO_5. The long-range and short-range structures of the as-prepared Li_2TiSiO_5 were characterized through X-ray Bragg diffraction and pair distribution analysis. The Bragg scattering data were collected at beamline 11-ID, Advanced Photon Source and was discussed in a separate work of ours.[53] The main phase of tetragonal Li_2TiSiO_5 (space group *P*4/*nmm*, #129) was verified, along with a small amount of SiO_2 (1.00 wt %) and TiO_2 (4.27 wt %) impurities. The crystal structure belongs to natisite family and is built up by layers of TiO_5 square pyramids and SiO_4 tetrahedra connected by corner sharing in *a*−*b* planes. These layers are stacked along the *c* lattice direction, and in-between every two of these layers lies a Li layer with distorted octahedral coordination (Figure 1). We

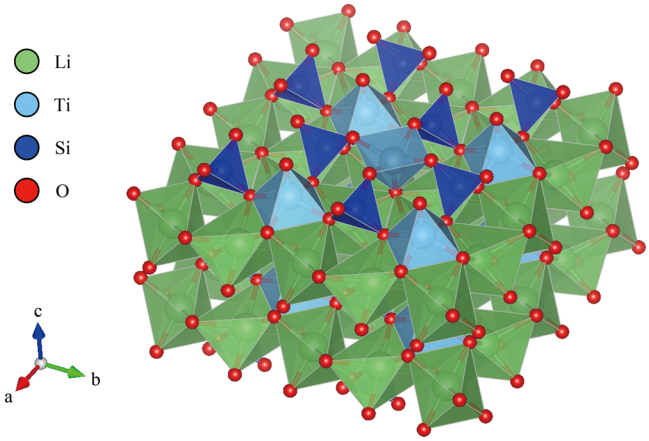

Figure 1. Crystal structure of Li_2TiSiO_5 displayed in a polyhedral representation of a 2 × 2 × 2 supercell by the software VESTA.[54]

note that the coordination environment of Ti atoms is different compared with those in simple lithium titanium oxides (*e.g.*, $Li_4Ti_5O_{12}$) which are either tetrahedrally or octahedrally coordinated. Titanium atoms in Li_2TiSiO_5 coordinate with five oxygen atoms forming square pyramids. The apical Ti−O bond distance is 1.671(3) Å, and the distance between Ti and four basal oxygen atoms is 1.973(1) Å, according to previous refinement.

Short-range structure of Li_2TiSiO_5 was probed through X-ray PDF, which again shows the square-pyramid coordination of Ti. Data were refined in the software package of PDFgui. PDF data in the range of 1.0−30.0 Å were fitted starting from the structural model obtained from Bragg diffraction of the

https://dx.doi.org/10.1021/acs.jpcc.0c10221
J. Phys. Chem. C 2021, 125, 3733−3744

previous work (Figure 2).[44] We note that the fitting quality below approximately 7 Å is worse than that of beyond, which

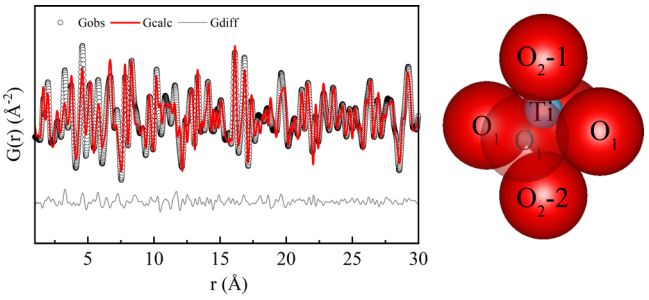

Figure 2. PDF $[G(r)]$ of Li_2TiSiO_5 and its fitting.

indicates the likely presence of amorphous impurity in the sample. Three distinct bond lengths of Ti−O bonds were visible in the $G(r)$ curve. One at 1.65 Å (corresponding to apical O atom), one at 1.98 Å (basal O atoms), and one at 2.69 Å (farther apical O atom), validating the structure model in which titanium atoms lie in square-pyramid coordination.

Calculated DOSs of the orbitals of the composing elements Li, Ti, Si, O and of Ti 3d orbitals and O 2p orbitals are presented in Figure 3a,b, respectively. It can be clearly observed from DOS that the valence band maximum is mainly contributed by O 2p orbitals, while the conduction band minimum is mostly contributed by Ti 3d orbitals (Figure 3a). Some lone pair electrons in O 2p orbitals reside below the Fermi level (−1 to 0 eV). While identical DOS peak characteristic at certain energy often infers orbital interactions, DOS peaks of Ti 3d and O 2p orbitals, as illustrated in Figure 3b, suggest interactions between all the five Ti 3d orbitals and O 2p orbitals. Slightly different from ideal square-pyramid coordination in which central atom located within the plane of four basal O atoms, distorted square pyramid in the crystal structure of Li_2TiSiO_5, leads to a 3d splitting in the order of $3d_{xy}$, $3d_{xz}/3d_{yz}$, $3d_{z^2}$, and $3d_{x^2-y^2}$ (from low to high energy), as revealed in Figure 3b. For ideal square pyramidal coordination where the central atom locates within the basal plane, 3d orbitals split as d_{xz}/d_{yz}, d_{xy}, d_{z^2}, $d_{x^2-y^2}$ (from lower to higher energy level). In Li_2TiSiO_5, where Ti is shifted above the basal plane, the apical O−Ti−basal O bond angle θ is no longer 90° but 107.7°. As a result, d_{z^2} and $d_{x^2-y^2}$ orbitals will have lower σ overlap with basal oxygen orbitals. In comparison, d_{xz}/d_{yz} orbitals interact more strongly with basal oxygen orbitals, leading to higher energy levels. The interaction between d_{xy} orbital and orbitals of basal O atoms, on the other hand, does not change much. Therefore, energy levels of d_{xz}/d_{yz} and d_{xy} in the square pyramidal coordination of Li_2TiSiO_5 are swapped in orders compared with that of Ti in an ideal square pyramidal coordination.[55,56]

Later, COHP analysis was performed to investigate the bonding interactions in details. Bonding interactions between Ti orbitals and orbitals of the apical O atom and basal O atoms were investigated. COHP results obtained for the atom pair of Ti atom and apical O atom (O_2-1) are given in Figure 4. Figure 4a shows the total COHP between Ti and apical O atom (O_2-1). With z directions pointing toward each other, and short atomic distance, Ti 3d orbitals that point toward z direction or have projections on the z direction are revealed to have strong interactions with O_2-1 2p orbitals (Figure 4b). At the valence band maximum, the interactions are pure Ti−O bonding, whereas above at the conduction band minimum are pure antibonding interactions, indicating electron occupation on Ti 3d−O 2p bonding orbitals. As for interactions between Ti 4p orbitals and O 2p orbitals, from the COHP results, there are obvious electron occupation on Ti 4p−O 2p bonding orbitals, mostly on $4p_x-2p_x$ and $4p_y-2p_y$ orbitals (Figure 4c). Interactions between Ti 3p and O 2p orbitals are also observed, where near the Fermi level, electrons occupy 3p−2p antibonding orbitals (Figure 4d). The interactions between other orbitals of Ti and O_2-1 are weak and are not displayed. Couples of equivalent molecular orbitals due to the symmetry are illustrated in the same line colors. In general, with the apical O atom, Ti 3d is observed to merely have strong σ

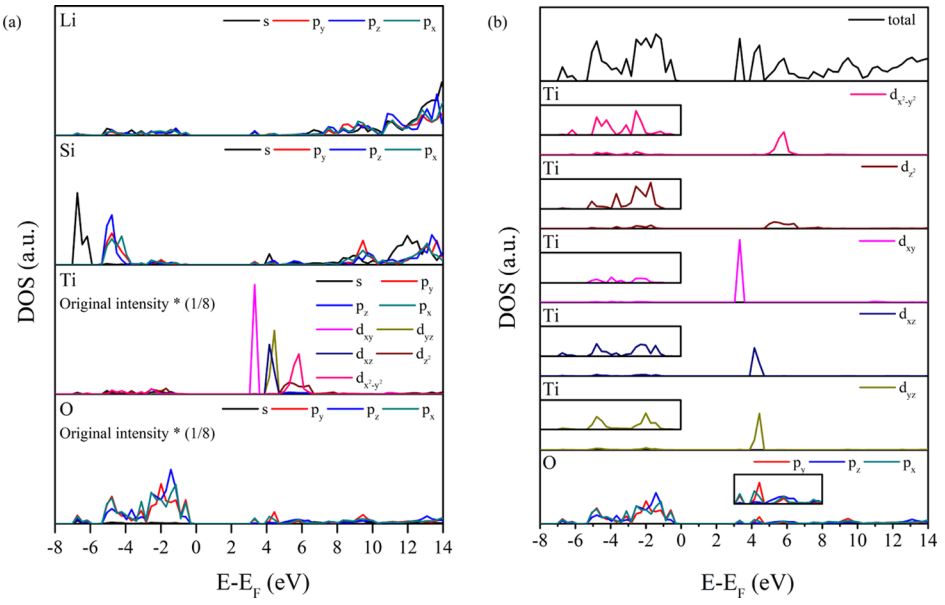

Figure 3. (a) DOSs of s and p orbitals of Li, Si, and O elements and s, p, and d orbitals of Ti in Li_2TiSiO_5 and (b) comparison between Ti 3d and O 2p orbitals, revealing orbital interactions.

https://dx.doi.org/10.1021/acs.jpcc.0c10221
J. Phys. Chem. C 2021, 125, 3733−3744

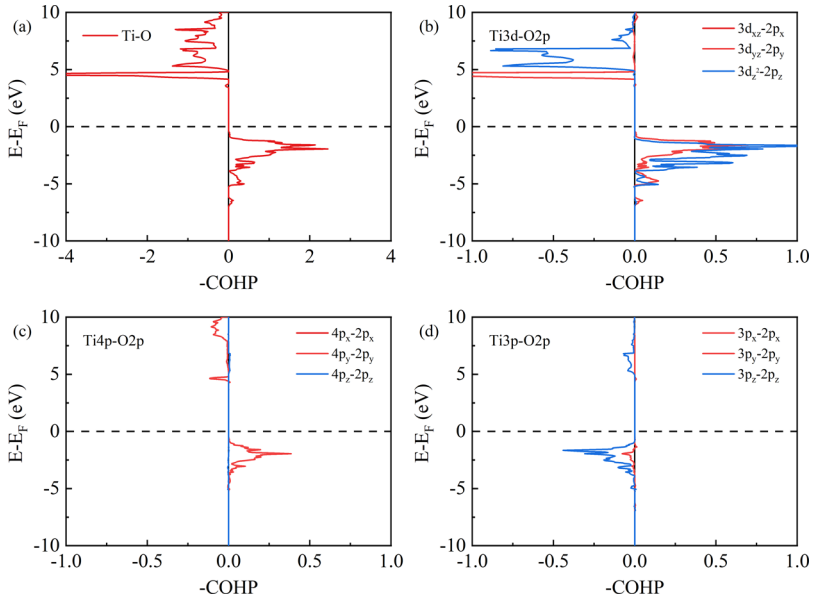

Figure 4. Results of COHP between (a) Ti and O2-1 in total, (b) Ti 3d orbital, and O2-1 2p orbitals, (c) Ti 4p orbital and O2-1 2p orbitals, and (d) Ti 3p orbital and O2-1 2p orbitals.

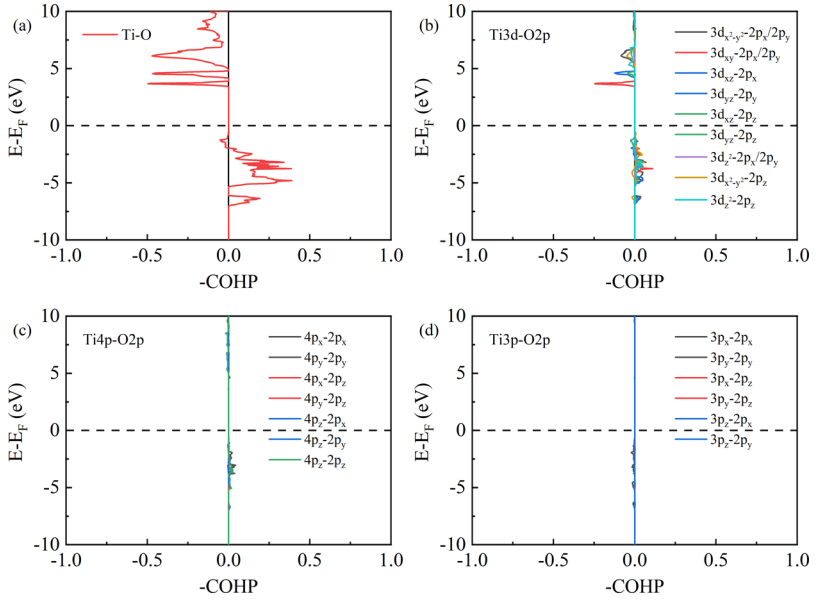

Figure 5. Results of averaged COHP between (a) Ti and O1 in total, (b) Ti 3d orbital and O1 2p orbitals, (c) Ti 4p orbital and O1 2p orbitals, and (d) Ti 3p orbital and O1 2p orbitals.

interactions. Both σ and π interactions are involved in 4p−2p and 3p−2p interactions.

Averaged orbital interactions of the basal O atoms with respect to central Ti atom are displayed in Figure 5. Figure 5a shows the total COHP between Ti and O_1. O 2p orbitals are shown to interact with all five Ti 3d orbitals to considerable extent (Figure 5b). Similar to the interactions between Ti 3d and O_2-1 2p orbitals, bonding and antibonding orbitals are formed. Moreover, electrons only occupy Ti 3d-O 2p bonding orbitals at the valence band maximum. Ti 4p and Ti 3p orbitals were revealed to have weak interactions with O_1 2p orbital (Figure 5c,d). The interactions between other orbitals of Ti and O_1 are insignificant and are not displayed. Couples of equivalent molecular orbitals due to the symmetry are illustrated in the same line colors. Different from the interactions with the apical O atom, the interactions with basal O atoms of Ti atom occur in a relatively indirect way due to limited overlap of Ti and O orbitals, resulting in lower COHP intensities.

In summary, focusing at the region right below the Fermi level, the valence band maximum is mainly composed of Ti 3d−O 2p bonding orbitals and some lone pair electrons in O 2p orbitals. The orbital of the lowest energy in conduction band is attributed to $3d_{xy}$ orbital of Ti, π interacting with O $2p_x/2p_y$ orbitals. For apical O atom and basal O atoms, they are observed to have distinct interactions with central Ti atom. Among Ti 3d orbitals, only ones that point along or have projections on the z direction ($3d_{xz}$, $3d_{yz}$, $3d_{z^2}$) have direct interactions with apical O atom. In comparison, all five Ti 3d orbitals participate in 3d−2p interactions with basal O atoms,

https://dx.doi.org/10.1021/acs.jpcc.0c10221
J. Phys. Chem. C 2021, 125, 3733−3744

but to smaller extents than that of between Ti and the apical O atom. What is identical for apical O atom and basal O atoms is that, electrons occupy Ti 3d−O 2p bonding orbitals at the valence band maximum, leaving Ti 3d−O 2p antibonding orbitals vacant. We will compare these orbital interactions with those of tetrahedrally and octahedrally coordinated Ti in the Discussion section.

Lithium Insertion Process in Li_2TiSiO_5. The discharge−charge curves, similar to a previous report,[44] are presented in Figure 6. With a specific current of 5 mA g^{-1} and cut-off

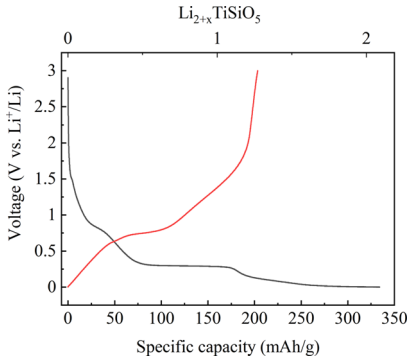

Figure 6. Cycling curves of Li_2TiSiO_5 for the first cycle at cut-off voltages of 0 and 3.0 V, at a specific current of 5 mA g^{-1}.

voltages of 0 and 3.0 V, the half-cells yield a discharge and charge specific capacity of approximately 334 and 203 mA h g^{-1}, respectively. A voltage plateau around 0.29 V was also observed. The origin of large irreversible capacity is still not fully understood. However, this is in part related to the solid-electrolyte interphase (SEI) formation process, which was discussed in a separate work of ours.[53]

Electronic structure and local coordination changes of titanium were followed by *ex situ* X-ray near-edge spectroscopy (XANES) and EXAFS. The X-ray absorption spectra collected were calibrated by a Ti foil spectrum and aligned according to the positions of pre-edge peaks. A complete X-ray absorption spectrum consists of pre-edge, edge, and post-edge features dependent on the energy compared to the K- or the L-edge probed. Pre-edge features originate from transitions toward empty bound states of electrons. For the first-period transition metal elements, the pre-edge peak corresponds to the 1s−3d electronic transition which is typically a dipole-forbidden transition. Depending on the extent that the 3d orbital is filled, pre-edge peak could have high or low intensities (slightly filled or heavily filled, respectively). That gives information on element type and/or element valence state. Another essential factor determining pre-edge features is a coordination environment. In octahedral coordination, 1s−3d transition is usually forbidden, resulting in a negligible pre-edge peak.[57−59] For tetrahedral coordination, on the contrary, 1s−3d transition yields sharp and intense pre-edge peak,[58−61] whereas five-fold coordination environments often lead to intermediate intensities of pre-edge peaks.[58,59,62] As shown in Figure 7, the intensity of pre-edge peak is substantially reduced when discharged below 0.7 V, suggesting that the coordination environment of Ti changes from square pyramid in pristine Li_2TiSiO_5 to octahedral-like coordination in lithiated Li_2TiSiO_5. Edge position provides valence information of Ti. Edge shift toward lower or higher energy indicates lower or higher valence state. From energies of Ti K-edges in the

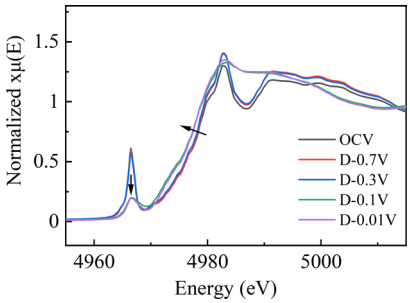

Figure 7. Ti K-edge X-ray absorption spectra of pristine and Li_2TiSiO_5 lithiated at various stages. Data were obtained at room temperature.

obtained spectra (Figure 7), a reduction from Ti(IV) to lower valence state within the plateau region was suggested. In contrast, in the voltage range from the open-circuit voltage (OCV) to 0.3 V, XANES features only had subtle changes. According to NMR and X-ray photoelectron spectroscopy results in our previous study of the same compound,[53] in the voltage regime from OCV down to 0.3 V, the surface component of Li_2CO_3 on Li_2TiSiO_5 particles continue to accumulate, while the oxidation state of Ti remains almost unchanged. We, therefore, believe that the electrochemistry in this voltage regime is dominated by SEI formation processes.

Right after absorption edge, there lies the extended edge of the post-edge region, which contains valuable information regarding local structure around Ti. With good-quality modeling, distances of nearest O neighbors in vicinity of Ti were obtained (Figure 8). In pristine Li_2TiSiO_5, atomic

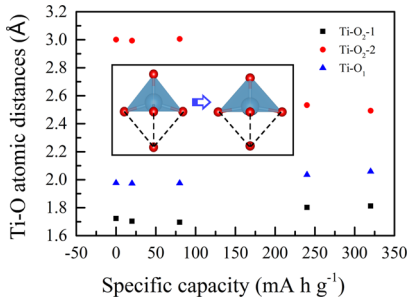

Figure 8. Bond length information calculated from EXAFS data.

distances were derived to be 1.805 Å for Ti−O pairs with apical oxygen atom (O_2-1) and 1.999 Å for other four Ti−O pairs with basal oxygen atoms (O_1). TiO_5 square pyramids in the structure of Li_2TiSiO_5 can be treated as greatly distorted octahedra, where one of the apical oxygen atoms (O_2-2) locates at too large distance to contribute electrons for bond interactions. As an approximation, a distorted octahedral model was established for modeling of EXAFS results, regardless of the reaction mechanism (*i.e.*, one-phase *vs* two-phase). Atomic distances of Ti−O pairs for Li_2TiSiO_5 samples lithiated to 20, 80, 240, and 320 mA h g^{-1} during discharge, that is, lithiation of Li_2TiSiO_5, were calculated and summarized. Details of fitting methodology and parameters are given in Supporting Information (Figures S1 and S2, Tables S1−S6). Atomic distances of Ti with both near and farther apical oxygen atoms and four coplanar oxygen atoms are displayed in Table 1. Analyzing the trend of Ti−O pair variations during lithiation, it can be observed that the strongly

https://dx.doi.org/10.1021/acs.jpcc.0c10221
J. Phys. Chem. C 2021, 125, 3733−3744

Table 1. Summary of Ti−O Bond Lengths of Samples at Various Lithiation Stages Derived from EXAFS Fitting

	specific capacity (mA h g^{-1})				
atomic distance (Å)	0 (OCV)	20 (0.7 V)	80 (0.3 V)	240 (0.1 V)	320 (0.01 V)
Ti−O_2-1	1.72	1.70	1.70	1.80	1.81
Ti−O_2-2	3.00	2.99	3.01	2.53	2.49
Ti−O_1	1.98	1.97	1.98	2.04	2.06

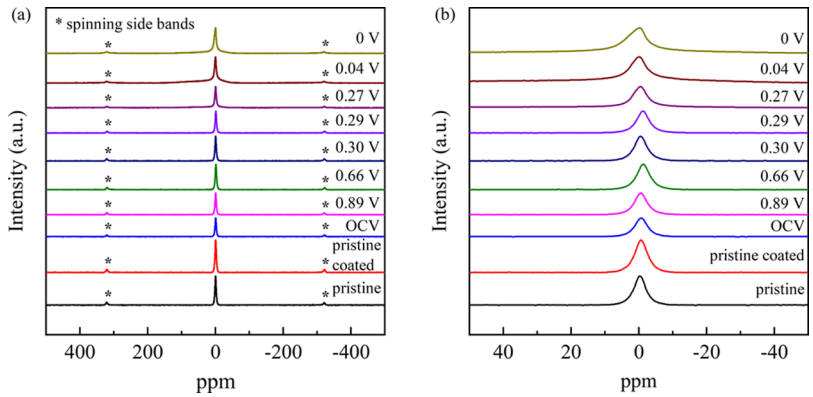

Figure 9. ^{7}Li MAS NMR spectra of Li_2TiSiO_5 samples at various stages of lithiation displayed (a) in the selected range of 500 to (−500) ppm and (b) in the vicinity of 0 ppm.

distorted octahedra tend to deform into less distorted ones, as illustrated in Figure 8 after the plateau region of electrochemistry. It is manifested as a reduction of Ti−O_2-2 atomic distance during lithium insertion. Atomic distances between Ti and apical (O_2-1) and basal (O_1) oxygen atoms are observed to subtly elongated during the same process. This expansion of distorted TiO_6 octahedron is in accordance with bond length increase often observed during transition-metal reduction in MO_6 octahedra.[63−69] In general, a less distorted TiO_6 octahedron resulted as Ti atom shifts toward the basal plane of square pyramid (or "octahedron center").

^{7}Li NMR directly probes local environments of inserted lithium. A series of samples taken during the process of lithiation were measured by ^{7}Li MAS NMR. ^{7}Li MAS NMR spectra of Li_2TiSiO_5 samples at various stages of lithiation were recorded between 2300 and −2300 ppm. Selected regions of 500 to −500 ppm are presented in Figure 9a, and those of 50 to −50 ppm zooming into the central resonance are presented in Figure 9b. In all samples, the spectra show a sharp resonance at 0 ppm (peak 1) which can be assigned to lithium in diamagnetic species. These species can be those with Ti^{4+} as in pristine Li_2TiSiO_5, diamagnetic secondary phases such as lithium silicate, or SEI compounds such as Li_2O, Li_2CO_3, and LiF.[70−72] Besides, a broad resonance at 30 ppm (peak 2) is observed to appear after discharging to voltages below 0.29 V, that is, at the plateau region. This broad resonance around 30 ppm indicates the existence of paramagnetic phase(s) containing most likely Ti^{3+} which agrees with the reduction of Ti(IV) to Ti(III) during lithiation. The appearance of broad peak at a lower ppm value due to increased paramagnetism of Ti(III) has also been reported for the $Li_4Ti_5O_{12}$ anode material.[73] Analyzing the integrated areas of the two components (*i.e.*, the 30 and 0 ppm resonance), the percentage of the paramagnetic phase first increases in the capacity region of 120−240 mA h g^{-1} (0.29−0.04 V), roughly the plateau region in the discharge curve, and then decrease in the region of 240−320 mA h g^{-1} (0.04−0 V), as displayed in Figure 10. Decrease of integrated area of peak 2 is observed to be accompanied with increase of integrated area of peak 1. One explanation would be during further Li insertion, paramagnetic Ti(III) phase decomposing into TiO and Li_2O or lithium silicate, the latter ones contributing to peak 1, rather than forming lithium-containing Ti(II) phase(s). Otherwise, the paramagnetism of Ti(II) phase would reveal itself in ^{7}Li MAS NMR. Another peak appearing at deep lithiation stages (peak 3 in Figure 10) can be attributed to the organic SEI product (alkyl carbonates ROCOOLi) generated at these lithiation stages. Such possibility is supported by a previous work of ours.[53] However, it remains elusive whether such organic carbonate species are only formed at deep lithiation stages or are formed at early lithiation stages but precipitate out of liquid electrolyte as their concentrations exceed solubility limits. The integrated area of peak 3 first increases and then remains approximately constant, in agreement with the formation process of ROCOOLi, as previously revealed.

In summary, according to structural characterizations [X-ray absorption spectroscopy (XAS), NMR] and our previous study of the same compound,[44] from OCV to the discharge plateau voltage (0.29 V), the discharge capacity is mostly contributed by SEI formation processes. The main product of this stage is Li_2CO_3 on the surface of Li_2TiSiO_5 particles.[53] Within the 0.3 V plateau region, a growth in the amount of paramagnetic phase(s) was captured by NMR, most likely the Ti(III) phase generated during lithiation and Li_2TiSiO_5 reduction. After the plateau and till full discharge, the significant change of the coordination environment of Ti revealed by XAFS fitting results and a decrease of paramagnetic resonance observed in ^{7}Li MAS NMR suggest a conversion process, possibly generating low-valence-state titanium oxide (*e.g.*, TiO) and diamagnetic phases such as Li_2O or lithium silicate.

DISCUSSION

The inductive effect has been widely investigated as means to increase lithium insertion voltage of electrode materials. In this work, we investigate the opposite side of the commonly known inductive effect, termed as reversed inductive effect. By

https://dx.doi.org/10.1021/acs.jpcc.0c10221
J. Phys. Chem. C 2021, 125, 3733−3744

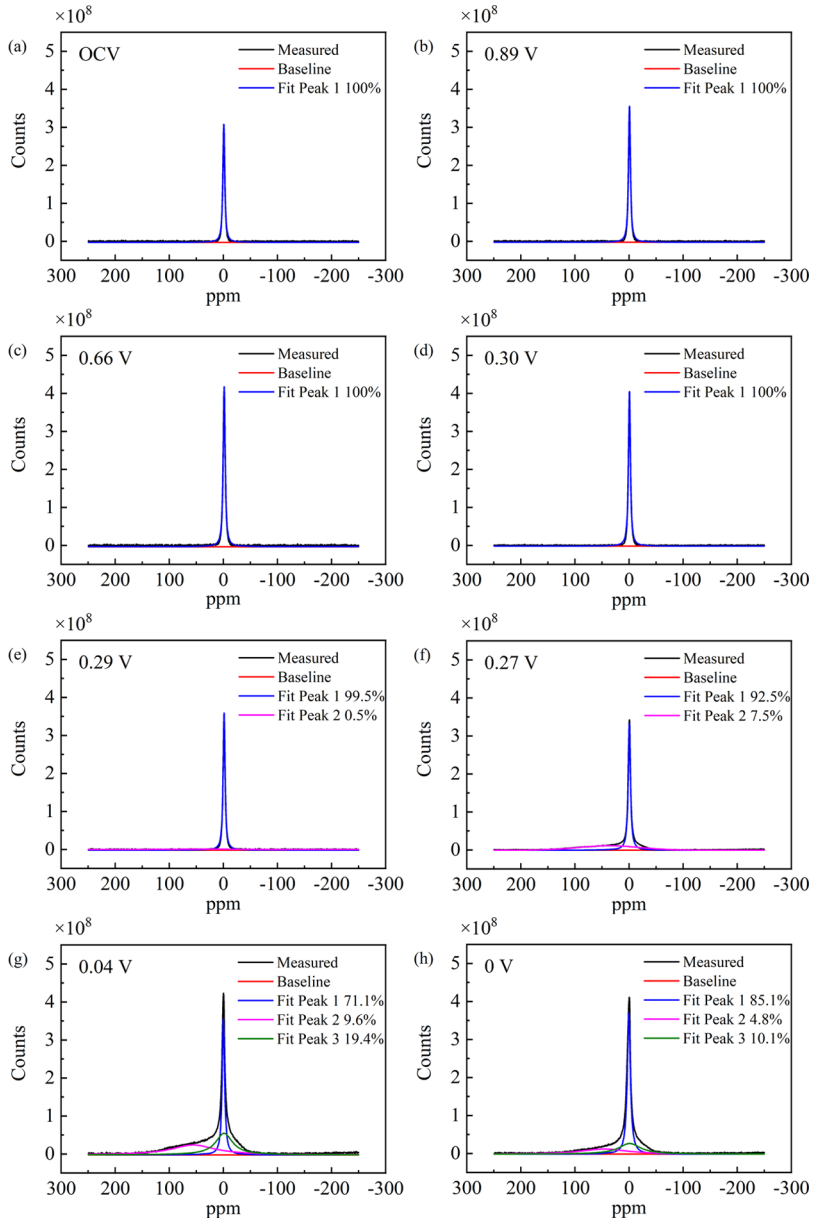

Figure 10. NMR fittings of samples at various lithiation stages.

structural characterizations, we determined the lithium insertion process of Li_2TiSiO_5 to be a complex one, consisting of sequential intercalation and conversion. From results obtained by DOS and COHP calculations, complicated interactions between Ti orbitals and apical and basal O orbitals were revealed as a probable origin of the observed reversed inductive effect. This is in stark contrast to octahedrally and tetrahedrally coordinated Ti. Low degree of degeneracy of 3d orbitals of transition metal in square-pyramid coordination is manifested as a rather complex splitting of 3d orbitals: $3d_{xy}$, $3d_{xz}/3d_{yz}$, $3d_{z^2}$, $3d_{x^2-y^2}$. Each was revealed to form a pair of bonding and antibonding orbitals with O 2p orbitals, in which apical and basal oxygen atoms contribute very differently. Consequently, molecular orbitals as compared with those in perfect octahedrally or tetrahedrally coordinated transition metals[74,75] are much more complex in TiO_5 square pyramids.

In octahedrally coordinated Ti, which is the most common coordination environment of Ti in inorganic compounds, degeneracy of Ti 3d orbitals is higher than that in square pyramids. Ti 3d orbitals split as $3d_{xy}/3d_{xz}/3d_{yz}$ (t_{2g}) and $3d_{x^2-y^2}/3d_{z^2}$ (e_g) (from low to high energy). Additionally, in octahedral coordination, t_{2g} orbitals often act as nonbonding molecular orbitals, leaving e_g orbitals the only Ti 3d orbitals involved in Ti 3d−O 2p interactions generating coupled bonding and antibonding orbitals. Due to the degeneracy, it is usually not needed to specifically distinguish which 3d orbital is exactly occupied by the highest-energy electron, or interactions with each individual ligand O atom. Tetrahedral coordination as another commonly observed coordination environment of Ti, for example, TiX_4 (X = halogen) and Ba_2TiO_4, has a high degree of degeneracy as well. Ti 3d orbitals split as $3d_{x^2-y^2}/3d_{z^2}$ (e) and $3d_{xy}/3d_{xz}/3d_{yz}$ (t_2) (from low to high energy). Ligands with lone pair electrons play an essential role in stabilizing tetrahedral coordination of ML_4 complexes of d^0 (electron-deficient) transition metals. A series of nonbonding orbitals contributed by Cl 3s and 3p lone pair electrons exist in molecular orbitals, for example, $TiCl_4$. Ti 3d

https://dx.doi.org/10.1021/acs.jpcc.0c10221
J. Phys. Chem. C 2021, 125, 3733−3744

orbitals and the rest Cl 3p orbitals form two groups of bonding−antibonding orbital pairs, that is, 3d−3p π bonding and antibonding (e) and 3d−3p σ/π bonding and antibonding (t_2).[76−78] Within T_d symmetry, σ and π t_2 orbitals are not separable.

The complex orbital interactions as observed in TiO_5 square pyramids further precludes the accurate analysis of molecular orbital changes during Ti(IV) reduction. The key of the following work would be to determine the type of orbital where the Ti^{4+}/Ti^{3+} redox couple resides, more specifically, whether the Ti^{4+}/Ti^{3+} redox couple resides on a bonding orbital or not. On the basis of preliminary insights obtained in this work, we expect that other titanium-based materials possessing the same natisite structure may exhibit relatively low electrochemical potentials as well, provided that lithiation and delithiation proceed through similar mechanisms. Reported compounds in the natisite structure include: $M(I)_2M(II)XO_5$ (M(I) = Li, Na, M(II) = Ti, V, X = Si, Ge). Even for sodium titanium oxide anodes with no polyanions present, extremely low sodium insertion potential (0.3 V *vs* Na^+/Na) has been observed in $Na_2Ti_3O_7$ in which titanium resides in a square pyramidal coordinated site[79] compared with octahedrally coordinated TiO_2 (0.7 V *vs* Na^+/Na), $NaTiO_2$ (0.9 V *vs* Na^+/Na), and $Na_2Ti_6O_{13}$ (0.9 V *vs* Na^+/Na).[80−83] This indicates that the unique electronic structure of square pyramidal TiO_5 may not only induce reversed inductive effect but also can itself serve as a low-potential redox center.

CONCLUSIONS

In summary, this work investigated the crystallographic and electronic structure of the anode material Li_2TiSiO_5 with a peculiarly low lithium insertion voltage for titanium-based anodes. Structural characterization tools were adopted verifying the square-pyramid coordination environment of titanium atoms with their ligand oxygen atoms. Additionally, the average coordination of Ti was observed to change toward distorted octahedral coordination during lithium insertion. A complex mechanism of Li_2TiSiO_5 lithiation was observed. Electronic structure and bonding characteristics were analyzed with help of DOS and COHP from DFT calculations. Complicated interactions between Ti orbitals and ligand O orbitals were revealed, in stark contrast with octahedral or tetrahedral coordination. Previously, the inductive effect has been only utilized to increase working potentials of electrode materials. Our results suggest that the reversed inductive effect also exists. Insights obtained in this work can provide new possibilities in designing future anode materials by tuning their working potentials to maximize energy density.

ASSOCIATED CONTENT

Supporting Information

The Supporting Information is available free of charge at https://pubs.acs.org/doi/10.1021/acs.jpcc.0c10221.

Calibration of Ti K-edge XAFS spectra, structural model for EXAFS fitting, EXAFS fitting results of samples at various lithiation stages, derived Ti−O interatomic distances, and other fitting parameters (PDF)

AUTHOR INFORMATION

Corresponding Authors

Hong Zhu − *University of Michigan-Shanghai Jiao Tong University Joint Institute, Shanghai Jiao Tong University, Shanghai 200240, China;* orcid.org/0000-0001-7919-5661; Email: hong.zhu@sjtu.edu.cn

Shou-Hang Bo − *University of Michigan-Shanghai Jiao Tong University Joint Institute, Shanghai Jiao Tong University, Shanghai 200240, China;* orcid.org/0000-0001-8963-5261; Email: shouhang.bo@sjtu.edu.cn

Yongyao Xia − *Department of Chemistry and Shanghai Key Laboratory of Molecular Catalysis and Innovative Materials, Institute of New Energy, iChEm (Collaborative Innovation Center of Chemistry for Energy Materials), Fudan University, Shanghai 200433, China;* orcid.org/0000-0001-6379-9655; Email: yyxia@fudan.edu.cn

Authors

Yifan Wu − *University of Michigan-Shanghai Jiao Tong University Joint Institute, Shanghai Jiao Tong University, Shanghai 200240, China;* orcid.org/0000-0003-1296-7035

Zhenming Xu − *University of Michigan-Shanghai Jiao Tong University Joint Institute, Shanghai Jiao Tong University, Shanghai 200240, China*

Yao Liu − *Department of Chemistry and Shanghai Key Laboratory of Molecular Catalysis and Innovative Materials, Institute of New Energy, iChEm (Collaborative Innovation Center of Chemistry for Energy Materials), Fudan University, Shanghai 200433, China;* orcid.org/0000-0001-5514-1917

Junchao Chen − *Key Laboratory of Mesoscopic Chemistry of MOE and Collaborative Innovation Center of Chemistry for Life Sciences, School of Chemistry and Chemical Engineering, Nanjing University, Nanjing 210023, China;* orcid.org/0000-0002-7601-5458

Luming Peng − *Key Laboratory of Mesoscopic Chemistry of MOE and Collaborative Innovation Center of Chemistry for Life Sciences, School of Chemistry and Chemical Engineering, Nanjing University, Nanjing 210023, China;* orcid.org/0000-0003-1935-1620

Olaf J. Borkiewicz − *Advanced Photon Source Sector 11-ID, Argonne National Laboratory, Argonne, Illinois 60439, United States*

Complete contact information is available at: https://pubs.acs.org/10.1021/acs.jpcc.0c10221

Author Contributions

The manuscript was written through contributions of all authors. All authors have given approval to the final version of the manuscript.

Notes

The authors declare no competing financial interest.

ACKNOWLEDGMENTS

This work was supported by the Shanghai Sailing Program (contract no. 18YF1411100), National Natural Science Foundation of China (grant nos. 21875045 and 22005059), and China Postdoctoral Science Foundation (grant no. 2019M661339). The authors thank the staff at Beamline BL14-W1 of SSRF for providing machine-hour of our X-ray absorption characterizations. Meanwhile, the authors would

like to thank Dr. Hao Liu at Beamline 11-ID for his support on X-ray PDF measurements. Use of the beamline at the Argonne National Laboratory was supported by the Office of Science of the U.S. Department of Energy (contract no. DE-AC02-06CH11357). Finally, discussion with Prof. Yong-Ning Zhou and Qin-Chao Wang from Fudan University on the interpretation of XAS data is greatly acknowledged.

REFERENCES

(1) Padhi, A. K.; Nanjundaswamy, K. S.; Masquelier, C.; Okada, S.; Goodenough, J. B. Effect of Structure on the Fe^{3+}/Fe^{2+} Redox Couple in Iron Phosphates. *J. Electrochem. Soc.* **1997**, *144*, 1609−1613.

(2) Padhi, A. K.; Nanjundaswamy, K. S.; Goodenough, J. B. Phospho-Olivines as Positive-Electrode Materials for Rechargeable Lithium Batteries. *J. Electrochem. Soc.* **1997**, *144*, 1188−1194.

(3) Kanno, R.; Shirane, T.; Kawamoto, Y.; Takeda, Y.; Takano, M.; Ohashi, M.; Yamaguchi, Y. Synthesis, Structure, and Electrochemical Properties of a New Lithium Iron Oxide, $LiFeO_2$, with a Corrugated Layer Structure. *J. Electrochem. Soc.* **1996**, *143*, 2435.

(4) Lee, Y. S.; Sato, S.; Tabuchi, M.; Yoon, C. S.; Sun, Y. K.; Kobayakawa, K.; Sato, Y. Structural Change and Capacity Loss Mechanism in Orthorhombic $Li/LiFeO_2$ System during Cycling. *Electrochem. Commun.* **2003**, *5*, 549−554.

(5) Hirayama, M.; Tomita, H.; Kubota, K.; Kanno, R. Structure and Electrode Reactions of Layered Rocksalt $LiFeO_2$ Nanoparticles for Lithium Battery Cathode. *J. Power Sources* **2011**, *196*, 6809−6814.

(6) Thackeray, M. M.; Johnson, P. J.; De Picciotto, L. A.; Bruce, P. G.; Goodenough, J. B. Electrochemical Extraction of Lithium from $LiMn_2O_4$. *Mater. Res. Bull.* **1984**, *19*, 179−187.

(7) Okubo, M.; Mizuno, Y.; Yamada, H.; Kim, J.; Hosono, E.; Zhou, H.; Kudo, T.; Honma, I. Fast Li-Ion Insertion into Nanosized $LiMn_2O_4$ without Domain Boundaries. *ACS Nano* **2010**, *4*, 741−752.

(8) Manthiram, A.; Goodenough, J. B. Lithium Insertion into $Fe_2(MO_4)_3$ Frameworks: Comparison of M = W with M = Mo. *J. Solid State Chem.* **1987**, *71*, 349−360.

(9) Manthiram, A.; Goodenough, J. B. Lithium Insertion into $Fe_2(SO_4)_3$ Frameworks. *J. Power Sources* **1989**, *26*, 403−408.

(10) Goodenough, J. B.; Kim, Y. Challenges for Rechargeable Li Batteries. *Chem. Mater.* **2009**, *22*, 587−603.

(11) Stock, L. M. The Origin of the Inductive Effect. *J. Chem. Educ.* **1972**, *49*, 400.

(12) Noll, W. The Silicate Bond from the Standpoint of Electronic Theory. *Angew. Chem., Int. Ed.* **1963**, *2*, 73−80.

(13) Recham, N.; Chotard, J.-N.; Dupont, L.; Delacourt, C.; Walker, W.; Armand, M.; Tarascon, J.-M. A 3.6 V Lithium-Based Fluorosulphate Insertion Positive Electrode for Lithium-Ion Batteries. *Nat. Mater.* **2010**, *9*, 68−74.

(14) Yamada, A.; Iwane, N.; Harada, Y.; Nishimura, S.-i.; Koyama, Y.; Tanaka, I. Lithium Iron Borates as High-Capacity Battery Electrodes. *Adv. Mater.* **2010**, *22*, 3583−3587.

(15) Legagneur, V.; An, Y.; Mosbah, A.; Portal, R.; La Salle, A. L. G.; Verbaere, A.; Guyomard, D.; Piffard, Y. $LiMBO_3$ (M = Mn, Fe, Co): Synthesis, Crystal Structure and Lithium Deinsertion/Insertion Properties. *Solid State Ionics* **2001**, *139*, 37−46.

(16) Nanjundaswamy, K.; Padhi, A.; Goodenough, J. B.; Okada, S.; Ohtsuka, H.; Arai, H.; Yamaki, J. Synthesis, Redox Potential Evaluation and Electrochemical Characteristics of NASICON-Related-3D Framework Compounds. *Solid State Ionics* **1996**, *92*, 1−10.

(17) Masquelier, C.; Padhi, A. K.; Nanjundaswamy, K. S.; Goodenough, J. B. New Cathode Materials for Rechargeable Lithium Batteries: The 3-D Framework Structures $Li_3Fe_2(XO4)_3$ (X = P, As). *J. Solid State Chem.* **1998**, *135*, 228−234.

(18) Chen, H.; Hautier, G.; Jain, A.; Moore, C.; Kang, B.; Doe, R.; Wu, L.; Zhu, Y.; Tang, Y.; Ceder, G. Carbonophosphates: A New Family of Cathode Materials for Li-Ion Batteries Identified Computationally. *Chem. Mater.* **2012**, *24*, 2009−2016.

(19) Liu, J.; Bao, Z.; Cui, Y.; Dufek, E. J.; Goodenough, J. B.; Khalifah, P.; Li, Q.; Liaw, B. Y.; Liu, P.; Manthiram, A.; et al. Pathways for Practical High-Energy Long-Cycling Lithium Metal Batteries. *Nat. Energy* **2019**, *4*, 180−186.

(20) Dahn, J. R.; Zheng, T.; Liu, Y.; Xue, J. S. Mechanisms for Lithium Insertion in Carbonaceous Materials. *Science* **1995**, *270*, 590−593.

(21) Ohzuku, T.; Iwakoshi, Y.; Sawai, K. Formation of Lithium-Graphite Intercalation Compounds in Nonaqueous Electrolytes and Their Application as a Negative Electrode for a Lithium Ion (Shuttlecock) Cell. *J. Electrochem. Soc.* **1993**, *140*, 2490.

(22) Tatsumi, K.; Iwashita, N.; Sakaebe, H.; Shioyama, H.; Higuchi, S.; Mabuchi, A.; Fujimoto, H. The Influence of the Graphitic Structure on the Electrochemical Characteristics for the Anode of Secondary Lithium Batteries. *J. Electrochem. Soc.* **1995**, *142*, 716.

(23) Zheng, T.; McKinnon, W. R.; Dahn, J. R. Hysteresis during Lithium Insertion in Hydrogen-Containing Carbons. *J. Electrochem. Soc.* **1996**, *143*, 2137.

(24) Takami, N.; Satoh, A.; Ohsaki, T.; Kanda, M. Lithium Insertion and Extraction for High-Capacity Disordered Carbons with Large Hysteresis. *Electrochim. Acta* **1997**, *42*, 2537−2543.

(25) Liu, Q.; Du, C.; Shen, B.; Zuo, P.; Cheng, X.; Ma, Y.; Yin, G.; Gao, Y. Understanding Undesirable Anode Lithium Plating Issues in Lithium-Ion Batteries. *RSC Adv.* **2016**, *6*, 88683−88700.

(26) Wang, H.; Zhu, Y.; Kim, S. C.; Pei, A.; Li, Y.; Boyle, D. T.; Wang, H.; Zhang, Z.; Ye, Y.; Huang, W.; et al. Underpotential Lithium Plating on Graphite Anodes Caused by Temperature Heterogeneity. *Proc. Natl. Acad. Sci. U.S.A.* **2020**, *117*, 29453.

(27) Hein, S.; Danner, T.; Latz, A. An Electrochemical Model of Lithium Plating and Stripping in Lithium Ion Batteries. *ACS Appl. Energy Mater.* **2020**, *3*, 8519−8531.

(28) Tallman, K. R.; Zhang, B.; Wang, L.; Yan, S.; Thompson, K.; Tong, X.; Thieme, J.; Kiss, A.; Marschilok, A. C.; Takeuchi, K. J.; et al. Anode Overpotential Control via Interfacial Modification: Inhibition of Lithium Plating on Graphite Anodes. *ACS Appl. Mater. Interfaces* **2019**, *11*, 46864−46874.

(29) Li, J.; Dahn, J. R. An in situ X-Ray Diffraction Study of the Reaction of Li with Crystalline Si. *J. Electrochem. Soc.* **2007**, *154*, A156−A161.

(30) Ryu, J. H.; Kim, J. W.; Sung, Y.-E.; Oh, S. M. Failure Modes of Silicon Powder Negative Electrode in Lithium Secondary Batteries. *Electrochem. Solid-State Lett.* **2004**, *7*, A306.

(31) Li, X.; Yang, Z.; Fu, Y.; Qiao, L.; Li, D.; Yue, H.; He, D. Germanium Anode with Excellent Lithium Storage Performance in a Germanium/Lithium−Cobalt Oxide Lithium-Ion Battery. *ACS Nano* **2015**, *9*, 1858−1867.

(32) Yoon, S.; Park, C.-M.; Sohn, H.-J. Electrochemical Characterizations of Germanium and Carbon-Coated Germanium Composite Anode for Lithium-Ion Batteries. *Electrochem. Solid-State Lett.* **2008**, *11*, A42.

(33) Courtney, I. A.; Dahn, J. R. Electrochemical and in situ X-Ray Diffraction Studies of the Reaction of Lithium with Tin Oxide Composites. *J. Electrochem. Soc.* **1997**, *144*, 2045.

(34) Chan, C. K.; Peng, H.; Liu, G.; McIlwrath, K.; Zhang, X. F.; Huggins, R. A.; Cui, Y. High-Performance Lithium Battery Anodes Using Silicon Nanowires. *Nat. Nanotechnol.* **2008**, *3*, 31.

(35) Goriparti, S.; Miele, E.; De Angelis, F.; Di Fabrizio, E.; Proietti Zaccaria, R.; Capiglia, C. Review on Recent Progress of Nanostructured Anode Materials for Li-Ion Batteries. *J. Power Sources* **2014**, *257*, 421−443.

(36) Ohzuku, T.; Ueda, A.; Yamamoto, N. Zero-Strain Insertion Material of $Li[Li_{1/3}Ti_{5/3}]O_4$ for Rechargeable Lithium Cells. *J. Electrochem. Soc.* **1995**, *142*, 1431.

(37) Yang, J.; Zhao, J.; Chen, Y.; Li, Y. Preparation and Characterization of $LiTi_2O_4$ Anode Material Synthesized by One-Step Solid-State Reaction. *Ionics* **2010**, *16*, 425−429.

(38) Kuhn, A.; Martín, M.; García-Alvarado, F. New Ramsdellites $LiTi_{2-y}V_yO_4$ ($0 \le y \le 1$): Synthesis, Structure, Magnetic Properties and

https://dx.doi.org/10.1021/acs.jpcc.0c10221
J. Phys. Chem. C 2021, 125, 3733−3744

Electrochemical Performances as Electrode Materials for Lithium Batteries. *J. Solid State Chem.* **2010**, *183*, 20−26.
(39) de Dompablo, M. E. A. y.; Morán, E.; Várez, A.; García-Alvarado, F. Electrochemical Lithium Intercalation in $Li_2Ti_3O_7$-Ramsdellite Structure. *Mater. Res. Bull.* **1997**, *32*, 993−1001.
(40) Chiba, K.; Kijima, N.; Takahashi, Y.; Idemoto, Y.; Akimoto, J. Synthesis, Structure, and Electrochemical Li-Ion Intercalation Properties of $Li_2Ti_3O_7$ with $Na_2Ti_3O_7$-Type Layered Structure. *Solid State Ionics* **2008**, *178*, 1725−1730.
(41) Kataoka, K.; Awaka, J.; Kijima, N.; Hayakawa, H.; Ohshima, K.-i.; Akimoto, J. Ion-Exchange Synthesis, Crystal Structure, and Electrochemical Properties of $Li_2Ti_6O_{13}$. *Chem. Mater.* **2011**, *23*, 2344−2352.
(42) Pérez-Flores, J. C.; Baehtz, C.; Hoelzel, M.; Kuhn, A.; García-Alvarado, F. Full Structural and Electrochemical Characterization of $Li_2Ti_6O_{13}$ as Anode for Li-Ion Batteries. *Phys. Chem. Chem. Phys.* **2012**, *14*, 2892−2899.
(43) Patoux, S.; Masquelier, C. Lithium Insertion into Titanium Phosphates, Silicates, and Sulfates. *Chem. Mater.* **2002**, *14*, 5057−5068.
(44) Liu, J.; Pang, W. K.; Zhou, T.; Chen, L.; Wang, Y.; Peterson, V. K.; Yang, Z.; Guo, Z.; Xia, Y. Li_2TiSiO_5: A Low Potential and Large Capacity Ti-based Anode Material for Li-Ion Batteries. *Energy Environ. Sci.* **2017**, *10*, 1456.
(45) Toby, B. H.; Von Dreele, R. B. GSAS-II: The Genesis of a Modern Open-Source All Purpose Crystallography Software Package. *J. Appl. Crystallogr.* **2013**, *46*, 544−549.
(46) Farrow, C. L.; Juhas, P.; Liu, J. W.; Bryndin, D.; Božin, E. S.; Bloch, J.; Proffen, T.; Billinge, S. J. L. PDFfit2 and PDFgui: Computer Programs for Studying Nanostructure in Crystals. *J. Phys.: Condens. Matter* **2007**, *19*, 335219.
(47) Ravel, B.; Newville, M. ATHENA, ARTEMIS, HEPHAESTUS: Data Analysis for X-Ray Absorption Spectroscopy Using IFEFFIT. *J. Synchrotron Radiat.* **2005**, *12*, 537−541.
(48) Kohn, W.; Sham, L. J. Self-Consistent Equations Including Exchange and Correlation Effects. *Phys. Rev.* **1965**, *140*, A1133.
(49) Monkhorst, H. J.; Pack, J. D. Special Points for Brillouin-Zone Integrations. *Phys. Rev. B: Solid State* **1976**, *13*, 5188.
(50) Dudarev, S. L.; Botton, G. A.; Savrasov, S. Y.; Humphreys, C. J.; Sutton, A. P. Electron-Energy-Loss Spectra and the Structural Stability of Nickel Oxide: An LSDA+U Study. *Phys. Rev. B: Condens. Matter Mater. Phys.* **1998**, *57*, 1505.
(51) Gao, Y.; Wang, X.; Ma, J.; Wang, Z.; Chen, L. Selecting Substituent Elements for Li-Rich Mn-Based Cathode Materials by Density Functional Theory (DFT) Calculations. *Chem. Mater.* **2015**, *27*, 3456−3461.
(52) Maintz, S.; Deringer, V. L.; Tchougréeff, A. L.; Dronskowski, R. LOBSTER: A Tool to Extract Chemical Bonding from Plane-Wave Based DFT. *J. Comput. Chem.* **2016**, *37*, 1030−1035.
(53) Wu, Y.; Bo, S.-H.; Xia, Y. Solid-Electrolyte Interphase Formation Process on Li_2TiSiO_5 Anode in $LiPF_6$-Based Carbonate Electrolyte. *J. Power Sources* **2020**, *467*, 228292.
(54) Momma, K.; Izumi, F. VESTA: A Three-Dimensional Visualization System for Electronic and Structural Analysis. *J. Appl. Crystallogr.* **2008**, *41*, 653−658.
(55) Craig, G. A.; Murrie, M. 3d Single-Ion Magnets. *Chem. Soc. Rev.* **2015**, *44*, 2135−2147.
(56) Albright, T. A.; Burdett, J. K.; Whangbo, M.-H. *Orbital Interactions in Chemistry*; John Wiley & Sons, 2013.
(57) Shinde, D. S.; Bhange, P. D.; Arbuj, S. S.; Kim, J.-Y.; Bae, J.-H.; Nam, K.-W.; Tayade, S. N.; Bhange, D. S. $NaFeTiO_4$: A Novel Visible Light Active Photocatalyst for Water Splitting and Environmental Remediation. *Int. J. Hydrogen Energy* **2020**, *45*, 8605−8617.
(58) Farges, F. Coordination of Ti in Crystalline and Glassy Fresnoites: A High-Resolution XANES Spectroscopy Study at the Ti K-Edge. *J. Non-Cryst. Solids* **1996**, *204*, 53−64.
(59) Farges, F.; Brown, G. E.; Navrotsky, A.; Gan, H.; Rehr, J. J. Coordination Chemistry of Ti(IV) in Silicate Glasses and Melts: II. Glasses at Ambient Temperature and Pressure. *Geochim. Cosmochim. Acta* **1996**, *60*, 3039−3053.
(60) Bordiga, S.; Bonino, F.; Damin, A.; Lamberti, C. Reactivity of $Ti_{(IV)}$ Species Hosted in TS-1 towards H_2O_2−H_2O Solutions Investigated by ab initio Cluster and Periodic Approaches Combined with Experimental XANES and EXAFS Data: A Review and New Highlights. *Phys. Chem. Chem. Phys.* **2007**, *9*, 4854−4878.
(61) Bosman, E.; Thieme, J. Modeling of XANES-Spectra with the FEFF-Program. *J. Phys.: Conf. Ser.* **2009**, *186*, 012004.
(62) Mastelaro, V. R.; Keding, R. X-Ray Absorption Spectroscopy Investigation of $Ba_2TiSi_2O_8$+xSiO_2 Glasses. *J. Non-Cryst. Solids* **2001**, *282*, 181−187.
(63) Petersburg, C. F.; Li, Z.; Chernova, N. A.; Whittingham, M. S.; Alamgir, F. M. Oxygen and Transition Metal Involvement in the Charge Compensation Mechanism of $LiNi_{1/3}Mn_{1/3}Co_{1/3}O_2$ Cathodes. *J. Mater. Chem.* **2012**, *22*, 19993−20000.
(64) Yoon, W.-S.; Balasubramanian, M.; Chung, K. Y.; Yang, X.-Q.; McBreen, J.; Grey, C. P.; Fischer, D. A. Investigation of the Charge Compensation Mechanism on the Electrochemically Li-Ion Deintercalated $Li_{1-x}Co_{1/3}Ni_{1/3}Mn_{1/3}O_2$ Electrode System by Combination of Soft and Hard X-Ray Absorption Spectroscopy. *J. Am. Chem. Soc.* **2005**, *127*, 17479−17487.
(65) Croy, J. R.; Balasubramanian, M.; Kim, D.; Kang, S.-H.; Thackeray, M. M. Designing High-Capacity, Lithium-Ion Cathodes Using X-Ray Absorption Spectroscopy. *Chem. Mater.* **2011**, *23*, 5415−5424.
(66) Kawaguchi, T.; Fukuda, K.; Tokuda, K.; Sakaida, M.; Ichitsubo, T.; Oishi, M.; Mizuki, J. i.; Matsubara, E. Roles of Transition Metals Interchanging with Lithium in Electrode Materials. *Phys. Chem. Chem. Phys.* **2015**, *17*, 14064−14070.
(67) Okumura, T.; Fukutsuka, T.; Yanagihara, A.; Orikasa, Y.; Arai, H.; Ogumi, Z.; Uchimoto, Y. Electronic and Local Structural Changes with Lithium-Ion Insertion in TiO_2-B: X-Ray Absorption Spectroscopy Study. *J. Mater. Chem.* **2011**, *21*, 15369−15377.
(68) Lafont, U.; Carta, D.; Mountjoy, G.; Chadwick, A. V.; Kelder, E. M. In situ Structural Changes upon Electrochemical Lithium Insertion in Nanosized Anatase TiO_2. *J. Phys. Chem. C* **2010**, *114*, 1372−1378.
(69) Borghols, W. J. H.; Lützenkirchen-Hecht, D.; Haake, U.; van Eck, E. R. H.; Mulder, F. M.; Wagemaker, M. The Electronic Structure and Ionic Diffusion of Nanoscale $LiTiO_2$ Anatase. *Phys. Chem. Chem. Phys.* **2009**, *11*, 5742−5748.
(70) Yamakawa, N.; Jiang, M.; Key, B.; Grey, C. P. Identifying the Local Structures Formed during Lithiation of the Conversion Material, Iron Fluoride, in a Li Ion Battery: A Solid-State NMR, X-ray Diffraction, and Pair Distribution Function Analysis Study. *J. Am. Chem. Soc.* **2009**, *131*, 10525−10536.
(71) Meyer, B. M.; Leifer, N.; Sakamoto, S.; Greenbaum, S. G.; Grey, C. P. High Field Multinuclear NMR Investigation of the SEI Layer in Lithium Rechargeable Batteries. *Electrochem. Solid-State Lett.* **2005**, *8*, A145−A148.
(72) Michan, A. L.; Leskes, M.; Grey, C. P. Voltage Dependent Solid Electrolyte Interphase Formation in Silicon Electrodes: Monitoring the Formation of Organic Decomposition Products. *Chem. Mater.* **2016**, *28*, 385−398.
(73) Tang, M.; Sarou-Kanian, V.; Melin, P.; Leriche, J.-B.; Ménétrier, M.; Tarascon, J.-M.; Deschamps, M.; Salager, E. Following Lithiation Fronts in Paramagnetic Electrodes with in situ Magnetic Resonance Spectroscopic Imaging. *Nat. Commun.* **2016**, *7*, 13284.
(74) Zhou, Y.-N.; Ma, J.; Hu, E.; Yu, X.; Gu, L.; Nam, K.-W.; Chen, L.; Wang, Z.; Yang, X.-Q. Tuning Charge−Discharge Induced Unit Cell Breathing in Layer-Structured Cathode Materials for Lithium-Ion Batteries. *Nat. Commun.* **2014**, *5*, 5381.
(75) Li, B.; Xia, D. Anionic Redox in Rechargeable Lithium Batteries. *Adv. Mater.* **2017**, *29*, 1701054.
(76) Nakatsuji, H.; Ehara, M.; Palmer, M. H.; Guest, M. F. Theoretical Study on the Excited and Ionized States of Titanium Tetrachloride. *J. Chem. Phys.* **1992**, *97*, 2561−2570.

https://dx.doi.org/10.1021/acs.jpcc.0c10221
J. Phys. Chem. C 2021, 125, 3733−3744

(77) Bursten, B. E.; Green, J. C.; Kaltsoyannis, N.; MacDonald, M. A.; Sze, K. H.; Tse, J. S. Variable Photon Energy Photoelectron Spectroscopic, and Theoretical Investigations of the Electronic Structure of $TiCl_4$. *Inorg. Chem.* **1994**, *33*, 5086−5093.
(78) Mousty-Desbuquoit, C.; Riga, J.; Verbist, J. J. Solid State Effects in the Electronic Structure of $TiCl_4$ Studied by XPS. *J. Chem. Phys.* **1983**, *79*, 26−32.
(79) Senguttuvan, P.; Rousse, G.; Seznec, V.; Tarascon, J.-M.; Palacín, M. R. $Na_2Ti_3O_7$: Lowest Voltage Ever Reported Oxide Insertion Electrode for Sodium Ion Batteries. *Chem. Mater.* **2011**, *23*, 4109−4111.
(80) Cech, O.; Castkova, K.; Chladil, L.; Dohnal, P.; Cudek, P.; Libich, J.; Vanysek, P. Synthesis and Characterization of $Na_2Ti_6O_{13}$ and $Na_2Ti_6O_{13}/Na_2Ti_3O_7$ Sodium Titanates with Nanorod-Like Structure as Negative Electrode Materials for Sodium-Ion Batteries. *J. Energy Storage* **2017**, *14*, 391−398.
(81) Wu, D.; Li, X.; Xu, B.; Twu, N.; Liu, L.; Ceder, G. $NaTiO_2$: A Layered Anode Material for Sodium-Ion Batteries. *Energy Environ. Sci.* **2015**, *8*, 195−202.
(82) He, H.; Sun, D.; Zhang, Q.; Fu, F.; Tang, Y.; Guo, J.; Shao, M.; Wang, H. Iron-Doped Cauliflower-Like Rutile TiO_2 with Superior Sodium Storage Properties. *ACS Appl. Mater. Interfaces* **2017**, *9*, 6093−6103.
(83) Kim, K.-T.; Ali, G.; Chung, K. Y.; Yoon, C. S.; Yashiro, H.; Sun, Y.-K.; Lu, J.; Amine, K.; Myung, S.-T. Anatase Titania Nanorods as an Intercalation Anode Material for Rechargeable Sodium Batteries. *Nano Lett.* **2014**, *14*, 416−422.

https://dx.doi.org/10.1021/acs.jpcc.0c10221
J. Phys. Chem. C 2021, 125, 3733−3744